

Global MHD Simulations of Cylindrical Keplerian Disks

John F. Hawley

*Virginia Institute for Theoretical Astronomy, Department of Astronomy, University of Virginia,
Charlottesville VA 22903*

ABSTRACT

This paper presents a series of global three dimensional accretion disk simulations carried out in the cylindrical limit in which the vertical component of the gravitational field is neglected. The simulations use a cylindrical pseudo-Newtonian potential, $\propto 1/(R - R_g)$, to model the main dynamical properties of the Schwarzschild metric. The radial grid domain runs out to $60 R_g$ to minimize the influence of the outer boundary on the inner disk evolution. The disks are initially constant density with a Keplerian angular momentum distribution and contain a weak toroidal or vertical field which serves as the seed for the magnetorotational instability. These simulations reaffirm many of the conclusions of previous local simulations. The MRI grows rapidly and produces MHD turbulence with a significant Maxwell stress which drives accretion. Tightly-wrapped low- m spiral waves are prominent. In some simulations radial variations in Maxwell stress concentrate gas into rings, creating substantial spatial inhomogeneities. As in previous global simulations, there is a nonzero stress at the marginally stable orbit. The stress is smaller than seen in stratified torus simulations, but nevertheless produces a small decline in specific angular momentum inside the last stable orbit. Detailed comparisons between simulations are used to examine the effects of various choices in computational setup. Because the driving instability is local, a reduction in the azimuthal computational domain to some fraction of 2π does not create large qualitative differences. Similarly, the choice of either an isothermal or adiabatic equation of state has little impact on the initial evolution. Simulations that begin with vertical fields have greater field amplification and higher ratios of stress to magnetic pressure compared with those beginning with toroidal fields. In contrast to MHD, hydrodynamics alone neither creates nor sustains turbulence.

Subject headings: accretion—accretion disks—instabilities—MHD—black holes

1. Introduction

Recent increases in supercomputer performance have significantly improved the ability to evolve the basic equations of accretion disk structure and evolution. These developments, along with continuing progress in understanding the most important physical processes that occur within

accretion disks, suggest that predictive disk simulations are a realistic goal. Such disk simulations will be global, fully three dimensional, and incorporate physical processes such as magnetohydrodynamics (MHD) and radiation transport. At present, we are some ways from this goal; global simulations are still rather idealized in terms of disk structure, energetics, and dynamical range. However, because almost any three dimensional disk simulation is relatively novel, there remain many significant questions to be investigated even with such simplified models.

To date there have been several global simulations of three dimensional disks, including Armitage (1998), Matsumoto (1999), Hawley (2000), Machida, Hayashi, & Matsumoto (2000), Hawley & Krolik (2001; hereafter HK), and Armitage, Reynolds & Chiang (2001; hereafter ARC). Much of this work has focused on thick accretion disks. With a pressure scale height H comparable to the disk radius R , the thick disk, or accretion torus, is more easily resolved in a numerical simulation than disks for which $H/R \ll 1$. Matsumoto (1999) followed the evolution of a thick torus embedded in an external vertical field, and found significant outflow collimated along the global vertical field lines. Hawley (2000) considered tori containing toroidal fields and poloidal field loops, and Machida et al. (2000) modeled a thick disk containing a toroidal field. In these studies the initial field was entirely contained within the disk and the resulting outflows were confined to the creation of a magnetized corona. A generic feature of all these thick disk simulations is the presence of large amplitude fluctuations in accretion rate, density, and other variables, in both space and time.

At a minimum these efforts have established that the magnetorotational instability, or MRI, (Balbus & Hawley 1991) is just as efficacious in thick disks as in local simulations to produce MHD turbulence and angular momentum transport. Thick accretion tori with initially non-Keplerian angular momentum distributions are highly unstable. MHD turbulence develops rapidly and is sustained by a self-consistent dynamo process within the disk. The constant or near-constant specific angular momentum distribution of the initial torus rapidly evolves to one that is near Keplerian. The main focus for dynamical studies would therefore seem to be Keplerian disks, both hot (high internal sound speed), and thin and cold (low internal sound speed).

Global simulations have been used to investigate specific physical issues in Keplerian accretion disk models. HK examined the behavior of a thick, nearly Keplerian disk model to study the accretion flow through the radius of the marginally stable orbit (r_{ms}) in a pseudo-Newtonian potential. They found significant stress at the location of the marginally stable orbit which creates a continuing decline in the value of the specific angular momentum ℓ inside of this point. The equation of state was adiabatic and there was no cooling, and the thickness of the disk remained roughly $H/R \sim 0.15$ throughout.

So far there have been fewer simulations of Keplerian disks with low internal sound speeds corresponding to small H/R . To sidestep the difficulty of resolving both H and R , the cylindrical disk limit has been employed which omits vertical gravity and stratification. Armitage (1998) and Hawley (2000) simulated a few examples of these cylindrically-symmetric Keplerian disks. More recently, ARC modeled several Keplerian cylindrical disks with sound speeds corresponding to H/R

of 0.08 and 0.04. They also computed one stratified disk that covered a limited vertical extent. As in the work of HK, they examined the inflow through r_{ms} . Although they found a nonzero Maxwell stress inside of r_{ms} , it was not large enough to alter ℓ to the same extent as seen in the simulation of HK. They emphasized that the differences between their simulations and those of HK were quantitative; the same dynamical effects were present, only at reduced amplitude. In addition to the lower initial sound speed and cylindrical symmetry, the ARC simulations used an angular domain of $\pi/6$ compared with the full 2π simulation of HK. It is unclear which, if any, of these differences is the most significant in comparing the results of HK and ARC.

Clearly, we still have only a preliminary understanding of the specific processes that establish the precise turbulent stress levels in disks. An attempt to investigate this question through simulation is further complicated by the need to distinguish between influences created purely by the numerical details (e.g. computational domain, numerical resolution, initial conditions), and those determined by physics. In an effort to characterize the array of technical choices in three dimensional simulations, this paper presents a series of disk simulations that begin with a Keplerian angular momentum distribution. These simulations are restricted to the cylindrical limit which omits the gravitational acceleration in the z direction. The cylindrical approximation has the distinct advantage of reducing the number of grid zones required in z : only the wavelengths of the weak-field MRI need be resolved, not several pressure scale heights. Here this advantage is exploited to increase the number of grid zones devoted to the radial extent of the disk, and its angular resolution.

Comparisons of cylindrical disks and vertically stratified disks in Hawley (2000) provided some evidence that the cylindrical disk is a good approximation for studying the evolution of density-averaged properties in a disk. Here we will be exploring the detailed properties and limitations of these cylindrical disks in greater detail. These cylindrical disks will be directly comparable to the simulations of ARC, and are the natural sequel to the local nonstratified shearing box simulations done previously (Hawley, Gammie, & Balbus 1995, hereafter HGB95; 1996; Matsumoto & Tajima 1995). Comparison with shearing boxes provide insight into those phenomena that are truly global versus those that are well-described locally. Cylindrical disk models will also provide a baseline of results that will be compared with future stratified Keplerian disk models.

Some of the questions that this investigation will address include: How do these global results compare with local shearing box simulations? Are there effects that can be attributed to influences from the equation of state, or which arise when compared to simulations of tori with higher internal temperatures? What differences are there in disks computed on grids with angular extent less than 2π ? Can a steady state be established in at least part of the disk? What are the amplitudes, and the time- and length-scales for the fluctuations that result from the MRI-induced turbulence?

The plan of this paper is as follows. In §2 the computational setup is described. Section 3 presents the results from a series of MHD cylindrical disk simulations. In §4 a purely hydrodynamic disk is considered for contrast. The results and their consequences are discussed in §5, and the

conclusions are summarized in §6.

2. Problem Setup

The simulations evolve the equations of ideal MHD,

$$\frac{\partial \rho}{\partial t} + \nabla \cdot (\rho \mathbf{v}) = 0, \quad (1)$$

$$\rho \frac{\partial \mathbf{v}}{\partial t} + (\rho \mathbf{v} \cdot \nabla) \mathbf{v} = -\nabla \left(P + \mathcal{Q} + \frac{B^2}{8\pi} \right) - \rho \nabla \Phi + \left(\frac{\mathbf{B}}{4\pi} \cdot \nabla \right) \mathbf{B}, \quad (2)$$

$$\frac{\partial \rho \epsilon}{\partial t} + \nabla \cdot (\rho \epsilon \mathbf{v}) = -(P + \mathcal{Q}) \nabla \cdot \mathbf{v}, \quad (3)$$

$$\frac{\partial \mathbf{B}}{\partial t} = \nabla \times (\mathbf{v} \times \mathbf{B}), \quad (4)$$

where ρ is the mass density, ϵ is the specific internal energy, \mathbf{v} is the fluid velocity, P is the pressure, \mathcal{Q} is an explicit artificial viscosity (Stone & Norman 1992a), \mathbf{B} is the magnetic field vector, and Φ is the gravitational potential. We employ cylindrical coordinates, (R, ϕ, z) , and work in the “cylindrical disk” limit which assumes a cylindrical gravitational potential and ignores vertical stratification. The gravitational potential Φ is a cylindrically-symmetric form of the Paczyński & Wiita (1980) pseudo-Newtonian potential $\Phi = -GM/(R - R_g)$. The equation of state is either isothermal, $P = c_s^2 \rho$, or adiabatic, $P = \rho \epsilon (\Gamma - 1)$. Radiation transport and losses are omitted. Since there is no explicit resistivity or physical viscosity, the adiabatic gas can heat only by compression, or in nonadiabatic heating through the action of the artificial viscosity \mathcal{Q} .

These equations are solved using time-explicit Eulerian finite differencing. The numerical algorithm is that employed by the ZEUS code for hydrodynamics (Stone & Norman 1992a) and MHD (Stone & Norman 1992b; Hawley & Stone 1995). Time and length units are established by setting $GM = R_g = 1$. To ensure a substantial reservoir of matter and to minimize the influence of the outer boundary, the radial grid runs from $R = 1.5$ to $R = 61.5$ using 256 radial grid zones. These grid zones are either evenly spaced, or graded so as to concentrate resolution in the inner regions. The azimuthal angle ϕ runs from 0 to some fraction of 2π depending upon the simulation. In the vertical direction z runs over a somewhat arbitrary periodic length. Periodic boundary conditions are employed in ϕ and z . The radial boundary conditions are simple zero-gradient outflow conditions; no flow into the computational domain is permitted. The radial magnetic field boundary condition is set by requiring the transverse components of the field to be zero outside the computational domain, while the perpendicular component satisfies the divergence-free constraint.

In the pseudo-Newtonian potential the angular momentum of a circular orbit (here referred to as the Keplerian angular momentum) is

$$\ell_{kep} = (GMR)^{1/2} \frac{R}{R - R_g} = \Omega R^2. \quad (5)$$

With $GM = R_g = 1$ the innermost marginally stable circular orbit r_{ms} is located at $R = 3$; at this point $\Omega = 0.29$, and the orbital period is $P_{orb} = 2\pi/\Omega = 21.8$. At the grid outer boundary the orbital period is almost 3000. The advantage of the large radius of the outer boundary is that many orbits can elapse in the inner regions of the disk before the outer boundary conditions become important to the simulation. This offers the possibility of establishing an accretion flow at the inner edge of the disk independent of the outer boundary condition (although still dependent of the initial conditions chosen for bulk of the disk).

In reporting results from the simulations many of the values will be averaged over both height z and angle ϕ . For example, the averaged mass density is

$$\langle \rho \rangle = \frac{\int \rho R d\phi dz}{\int R d\phi dz}. \quad (6)$$

The net local mass flux is

$$\langle \dot{M} \rangle = \int -\rho v_R R d\phi dz, \quad (7)$$

here defined to be positive for net accretion (inflow). Similar averages are constructed for pressure, magnetic energies, stresses and angular momentum. These averaged values are computed at specific time intervals. Where desired one can further average these quantities over time.

A drawback to reporting space and time averaged values is that they blur a very real and important property of the flow: it is highly variable. One way to measure the azimuthal fluctuation level at a given time is with the quantity

$$\frac{\delta\rho}{\rho}(R) = \frac{1}{\langle \rho \rangle} \left\{ \frac{1}{2\pi} \int d\phi [\rho - \langle \rho \rangle]^2 \right\}^{1/2}, \quad (8)$$

where $\langle \rho \rangle$ is defined in (6).

The azimuthal structure in the disk is examined with a fourier transform of a vertically averaged value such as density, e.g.,

$$\tilde{\rho}(R, m) = \frac{1}{2\pi} \int_0^{2\pi} \int_{-z_{max}}^{z_{max}} \rho(R, \phi, z) e^{im\phi} dz d\phi. \quad (9)$$

The power, $|\tilde{\rho}|^2$, is further averaged over radius within the interior of the active region in the disk. Similarly, the time-dependent behavior of a disk is examined with a fourier transform over time of azimuthally and vertically averaged values.

Table 1 lists the simulations carried out as part of this study. The models are identified by labels: CK stands for cylindrical Keplerian, HK for hydrodynamic Keplerian, and NK for Newtonian Keplerian, two models that use the standard $1/R$ Newtonian potential rather than the pseudo-Newtonian potential. The table also lists the computational domain, grid resolution, equation of state, initial field topology, and end time in code units.

3. Simulation Results

3.1. Disk with initial toroidal field

The first Keplerian disk simulation, CK5, considers a disk with an inner edge at $R = 10$, set back from r_{ms} . This will investigate disk accretion removed from the dynamical forces associated with the pseudo-Newtonian potential's innermost circular orbit. The simulation follows the global development of the MRI, turbulent angular momentum transport, and the resulting gradual accretion of matter and inward drift of the disk edge.

The initial conditions consist of an isothermal gas at constant density, $\rho = 1$, and a sound speed $c_s = 0.03054$ which gives a Mach number $\mathcal{M} = v_\phi/c_s = 11.5$ at $R = 10$. With the decrease in velocity v_ϕ the Mach number declines to 4.3 by the outer radial boundary. The azimuthal angle ϕ runs from 0 to $\pi/2$ in 58 grid zones, and in the vertical direction z runs from 0 to 2 in 24 grid zones. The vertical scale height at $R = 10$ corresponds to 0.87. Of course in the cylindrical disk approximation the absence of a vertical gravitational force means that the scale height has no hydrodynamical significance in z ; it is merely a convenient expression of the temperature of the disk in terms of the ratio of the sound speed to orbital frequency.

With a magnetic field, the vertical domain size retains significance even in the cylindrical disk limit in relation to the most unstable wavelength of the MRI. The magnetic field strength determines this wavelength, and the initial pressure determines the value of $P/P_{mag} \equiv \beta$ to which this field strength corresponds. For CK5 the initial magnetic field is purely toroidal with $\beta = 4$. For this strength of field the ratio of the Alfvén speed to the orbital frequency, v_A/Ω , ranges from 0.6 at the inner disk boundary to 10.2 at $R = 60$. The critical azimuthal wavenumber for the MRI, $m = R\Omega/v_A$, ranges from 16 at the inner disk to 6 at the outer boundary. Since the azimuthal direction spans $\pi/2$ with 58 grid zones, only wavenumbers $4 \leq m \leq 116$ will be realizable. With the chosen magnetic field strength, however, the unstable azimuthal wavenumbers of the MRI should be well resolved throughout the disk.

The simulation is run out to time $t = 3972$ which is 22 orbits at the disk's initial inner boundary, and 180 orbits at r_{ms} . As the simulation proceeds the MRI develops, first at the inner disk edge and spreading outward through the disk as time advances. Small wavelength perturbations (large m) grow most rapidly, but the largest azimuthal scales dominate in the end. The exponential growth of the poloidal field at a given radius ends after approximately five orbits, as measured locally. The Maxwell stress in the resulting MHD turbulence transports angular momentum and the disk evolves. Figure 1 shows a spacetime (R, t) plot of the Maxwell stress, $M^{R\phi}$, in terms of a Shakura & Sunyaev (1973) α using the initial pressure as a normalization, $\alpha = M^{R\phi}/\rho c_s^2$. This plot illustrates the rapid local buildup of magnetic stress to significant levels, as well as the large fluctuations in time and space.

Overall, the disk never attains a steady state; its inner edge slowly moves inward and fluid in the outer disk moves outward. Through the course of the simulation the disk inner edge moves

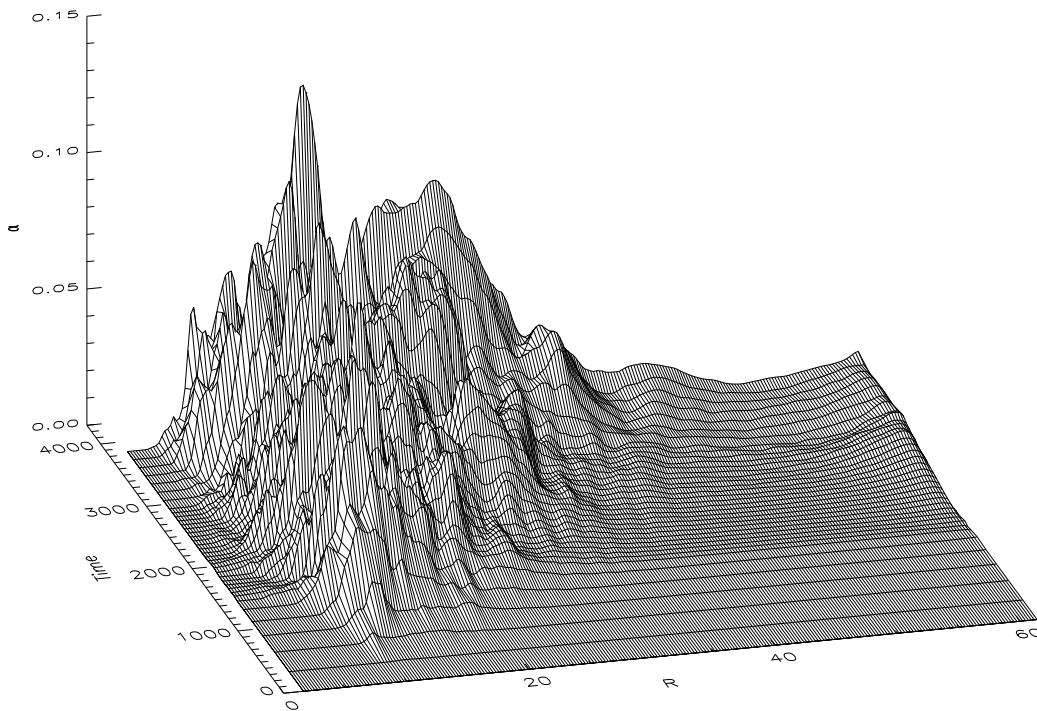


Fig. 1.— Spacetime diagram of the Maxwell stress in run CK5 normalized by the initial pressure $\alpha = M^{R\phi} / \rho c_s^2$. The stress develops first at $R = 10$ and then spreads out through the disk as the MRI grows at a rate proportional to the local orbital frequency. At the end of the simulation the stress rises rapidly from near zero at $R = 5$, reaches the highest levels between $R = 15$ and 30 , then declines rapidly with radius. Within the disk the stress varies strongly in both time and space.

from $R = 10$ down to $R = 5$. This is illustrated in Figure 2 which shows $\langle \rho \rangle$ at several times during the run. At the end time, the disk has not quite reached r_{ms} and there is no significant mass flux through the marginally stable orbit and into the central hole. Magnetic field has been carried inward along with the mass. The regions with the strongest fields lie between the peaks in the density distribution. The average β value varies between 8 at the density peaks and 2 in between.

Averaged properties of the accretion flow within the disk can be derived from a region between $R = 13$ and 22 which comes into an approximate time-averaged steady state after $t = 2800$. The time-averaged accretion rate within this region is roughly constant with radius, with $\dot{M} = 0.075$, and $v_R/v_\phi = -0.006$. The instantaneous fluctuations in radial velocity, $\delta v_R/v_\phi$ typically range between 0.01 and -0.02 . Within the turbulent disk the toroidal field energy dominates over that of the poloidal field, with the ratio $B_\phi^2/B_R^2 = 13$. The radial field energy is, in turn, a factor of 6 greater than the that of the vertical field. The toroidal field energy is essentially unchanged in the mean from its initial value, although there are spatial variations in strength by a factor of two within the disk. At the end of the run the region of significant Maxwell stress has moved out to around $R = 40$ with the largest values lying between $R = 7$ and 30 (Fig. 1). The time-averaged Maxwell stress over this range is about 5.5×10^{-5} , corresponding to an average value of $\alpha = 0.07$. The relatively low level of the radial field compared to the toroidal is reflected in the value of α_{mag} , the ratio of the Maxwell stress to the total *magnetic* pressure ($\alpha = \alpha_{mag}/\beta$). In the inner disk this value ranges between 0.2 and 0.3. The toroidal field simulation of ARC obtained an α slightly below 0.01, and an $\alpha_{mag} \sim 0.3$. (Note that there are differences in α terminology between this paper and ARC.)

The averaged magnetic properties of the turbulence are consistent with the results of toroidal field local shearing box simulations (cf. Table 3 of HGB95). For those simulations α was typically a few times 0.01, and $\alpha_{mag} \sim 0.4$ for simulations that began with weak toroidal fields and ~ 0.2 for those that began, like this simulation, with stronger toroidal fields.

3.2. Disk with initial vertical field

The two general classes of models considered in the local shearing box limit by HGB95 were initial vertical fields and initial toroidal fields. In the next simulation, CK6, we complete the extension of these local models from the shearing box to the cylindrical disk by simulating the same disk as CK5, but now with an initial vertical magnetic field.

Simulation CK6 is a Keplerian disk consisting of an isothermal gas at constant density $\rho = 1$ from $R = 10$ to the outer boundary, and a constant sound speed $c_s = 0.03054$. The radial grid resolution is the same as in CK5, but a few additional zones are added in the ϕ and z direction; ϕ runs from 0 to $\pi/2$ over 64 grid zones, and z runs from 0 to 2 in 32 grid zones. In CK6 the strength of the initial vertical magnetic field is set by requiring $2\pi v_A/\Omega = 0.5$ at every radius. This is nearly

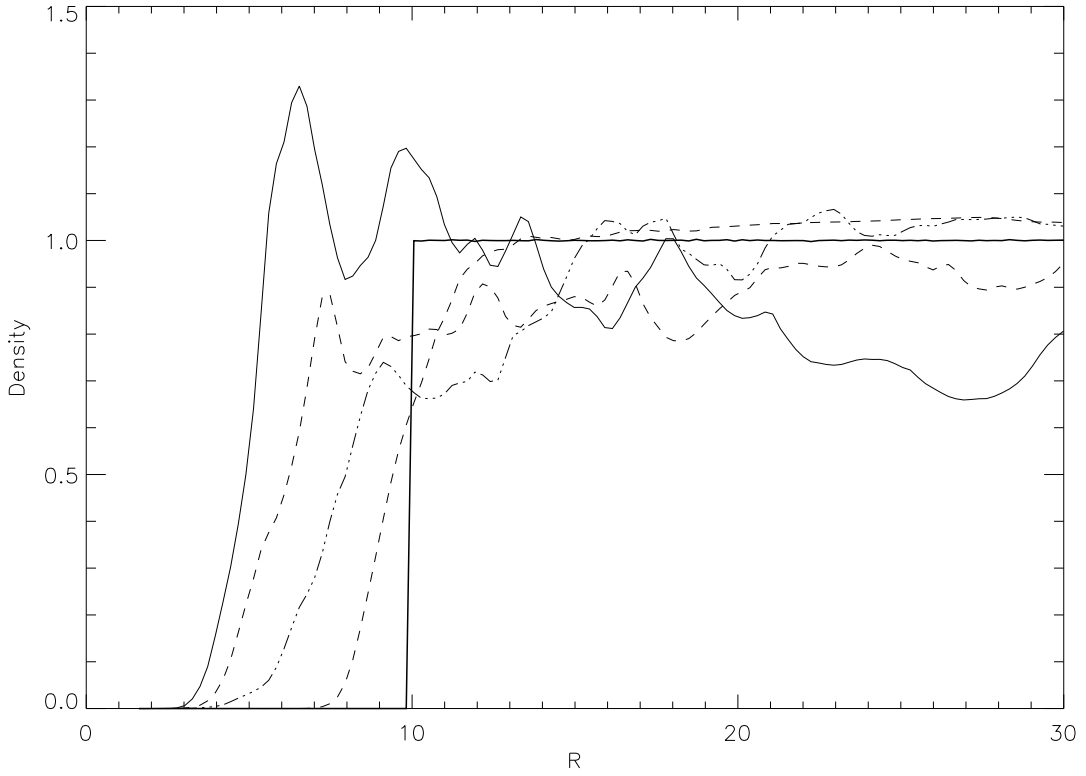


Fig. 2.— Radial profile of density $\langle \rho \rangle$ at times $t = 0$ (solid bold line), 890 (short dashed line), 1835 (dash-dotted line), 2734 (thick dashed line), 3848 (solid thin line) in simulation CK5. These times correspond to 0, 4.9, 10.2, 15.2, and 21.5 orbits at $R = 10$. Angular momentum transport produced by MHD turbulence causes the inner edge of the disk to drift gradually inward.

the fastest growing wavelength of the linear MRI; there will be four such wavelengths across the z domain. The initial magnetic field decreases with radius (proportional to Ω), with values of β ranging from 240 at the inner edge of the disk to 66,000 at the outer grid boundary. Although the most unstable vertical wavelength is the same throughout the disk, the local growth rate of the MRI is proportional to the local orbital frequency, so the magnetic instability grows more slowly with increasing radius.

The simulation is run out to time $t = 4097$ which is 22.9 orbits at the disk’s initial inner boundary ($R = 10$), 188 orbits at r_{ms} , and only 1.37 orbits at the grid outer boundary. As in CK5, MHD turbulence develops first in the inner disk and spreads outward. In CK6 the instability grows more rapidly, and although the field is much weaker initially, it still grows to about the same level as in CK5.

In CK6 accretion is driven through the marginally stable orbit at early time. This is due, in part, to a unique property of the vertical field instability. Large fluctuations and impulsive accretion are created by the “channel solution” of the nonlinear vertical field instability (Hawley & Balbus 1992; HGB95). The fastest growing modes have finite vertical wavenumber k_z and vanishing radial and azimuthal wavenumbers, k_R and m . This leads to coherent radial flow upon nonlinear saturation. Although the development of full turbulence eventually limits the coherence of this radial channel flow, early on in the simulation at the inner edge of the disk radial filaments of gas are able to move rapidly inward and accrete.

As the simulation proceeds, an interesting structure emerges in the inner part of the disk. By $t = 2000$ gas has piled up in a density maximum located at $R = 7.5$ and in a smaller maximum at $R = 4$. Between these rings are local minima at $R = 5$ and $R = 10$. These can be seen in Figure 3, a spacetime diagram of the vertically- and azimuthally-averaged density. For clarity, only the inner half of grid is shown and only up to $t = 2000$. A local maximum in density corresponds to a local minimum in the Maxwell stress and the Alfvén speed and vice versa. As time proceeds, the inner density maximum accretes into the hole, while the other slowly drifts inward, reaching $R = 4.2$ by $t = 4096$. By this time another density gap is opening up near $R = 17$.

The specific angular momentum, density, and Maxwell stress at the end time are shown in Figure 4. The Maxwell stress, and hence the angular momentum transport, is larger in regions of low density. The radial slope of the specific angular momentum ℓ becomes steeper in the regions of maximum Maxwell stress, and flatter in the density maxima. Essentially, the disk is forming a local pressure-supported slender torus with non-Keplerian angular momentum distribution to balance the internal pressure forces. Gas moves rapidly out of the region between the rings, but is blocked from further accretion by the torus itself. Thus there is a tendency for material to concentrate into rings.

The presence of dense rings and empty gaps is a description of the behavior of a “viscous-type” instability (Lightman & Eardley 1974) where the stress is a decreasing function of the density. Here the cause of this behavior is different from that considered originally by Lightman and Eardley

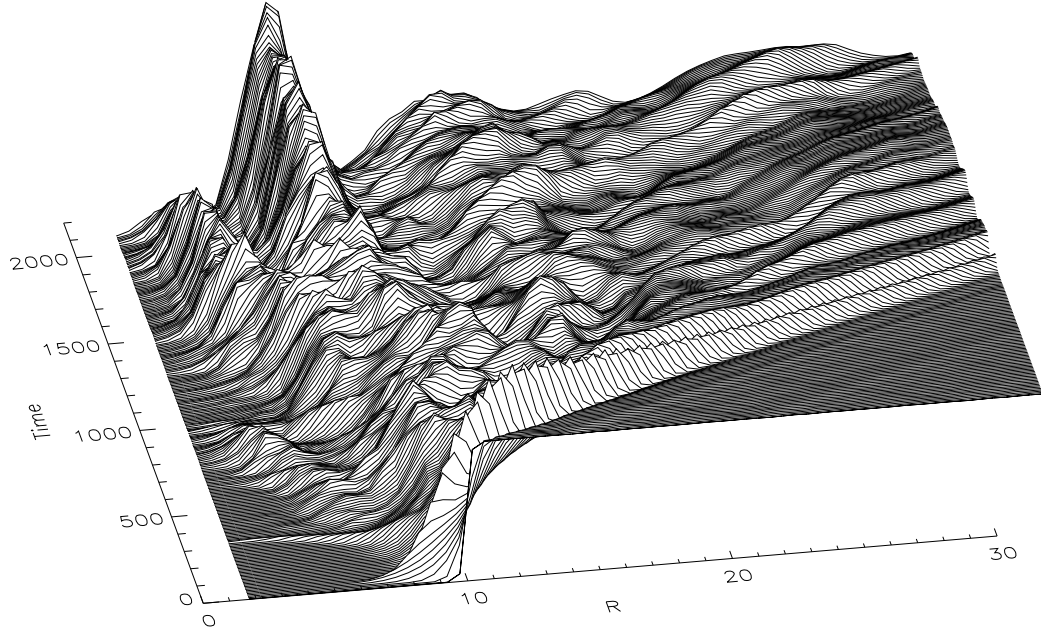


Fig. 3.— (R, t) spacetime diagram of the vertically and azimuthally averaged density $\langle \rho \rangle$ in simulation CK6 for the inner half of the radial grid from $t = 0$ to 2000. The disk is not initially in hydrostatic equilibrium at the inner edge, resulting in an outward traveling wave after $t = 0$. The turbulence itself subsequently generates magnetoacoustic waves. Of particular interest are the local density maxima and the gaps surrounding them which develop after $t = 1000$ at $R = 5$ and $R = 10$.

(1974). It is not a property of the Maxwell stress *per se* as much as it is a consequence of the properties of the MRI. Lower density corresponds to larger Alfvén speeds which, in turn, produce faster growth rates at larger wavelengths of the MRI. Longer wavelengths are more efficacious in transporting larger amounts of angular momentum.

A spacetime plot of the accretion rate shows evidence for significant time variability and periodicity. The variability is manifest as pressure waves that propagate throughout the disk at the sound speed. A fourier transform of the spacetime data reveals peaks in the power spectrum which originate at various radii in the disk. The peaks occur where the pressure waves are generated at frequencies close to the local orbital frequency. Initially the largest peak in the spectral energy is found close to $R = 13$; this is also where the peak Maxwell stress is generated. At late time the most prominent frequency observed corresponds to the orbital frequency at the location of the dense inner ring. This, in turn, drives a periodic accretion flux into the central hole.

The substantial spatial inhomogeneity of the disk at late time makes it difficult to assign overall “steady state” values to quantities. The azimuthal density fluctuations, characterized by (8) are as large as 0.3 in the region of maximum Maxwell stress, and are between 0.1 and 0.2 throughout the bulk of the radial extent of the disk. This level is comparable to that seen in the toroidal field simulation CK5. What sets CK6 apart are the large variations with radius.

The magnetic field has undergone substantial amplification. At the end of the run β is about 70 inside the dense ring at $R = 4$, and falls to 0.2 in the low density region at $R = 7$. From $R = 10$ to 40, β has a minimum of 14, with a local maximum ~ 70 at $r = 20$. Beyond $R = 30$ β slowly rises with radius to around 100 at the outer boundary. As stated above, the Maxwell stress is largest between the dense rings. The Shakura-Sunyaev α is as low as 0.002 in the inner ring, rising to ~ 4 at $R = 7$ before dropping back to values ranging from 0.01 to 0.05 between $R = 10$ and 40. As in run CK5 the average total toroidal field energy dominates over that of the poloidal field, although here by a lesser amount, with $B_\phi^2/B_R^2 = 6.3$. The radial field energy is a factor of 6 greater than the vertical field energy. The ratio of the Maxwell stress to the magnetic pressure, α_{mag} , varies with radius, but has an average of 0.5. This is larger than seen in CK5, and is the typical value for local shearing box simulations with a net vertical field.

3.3. Disk near the marginally-stable orbit

The recent work of HK and ARC focused on the stress at and interior to the marginally stable orbit. Having considered disks with inner boundaries located outside of r_{ms} , we now turn to a model, CK7, a disk with an initial inner edge near r_{ms} that produces substantial accretion into the central hole. It uses an adiabatic equation of state with $\Gamma = 5/3$. The computational grid extends from $R = 1.5$ to $R = 61.5$, over 0.8 in z , and 2π in ϕ . There are 32 equally spaced zones in z , 256 equally spaced zones in ϕ , and 256 zones in R . Eighty of the radial zones are equally spaced between $R = 1.5$ and 10, while the remainder are logarithmically stretched between 10 and 61.5.

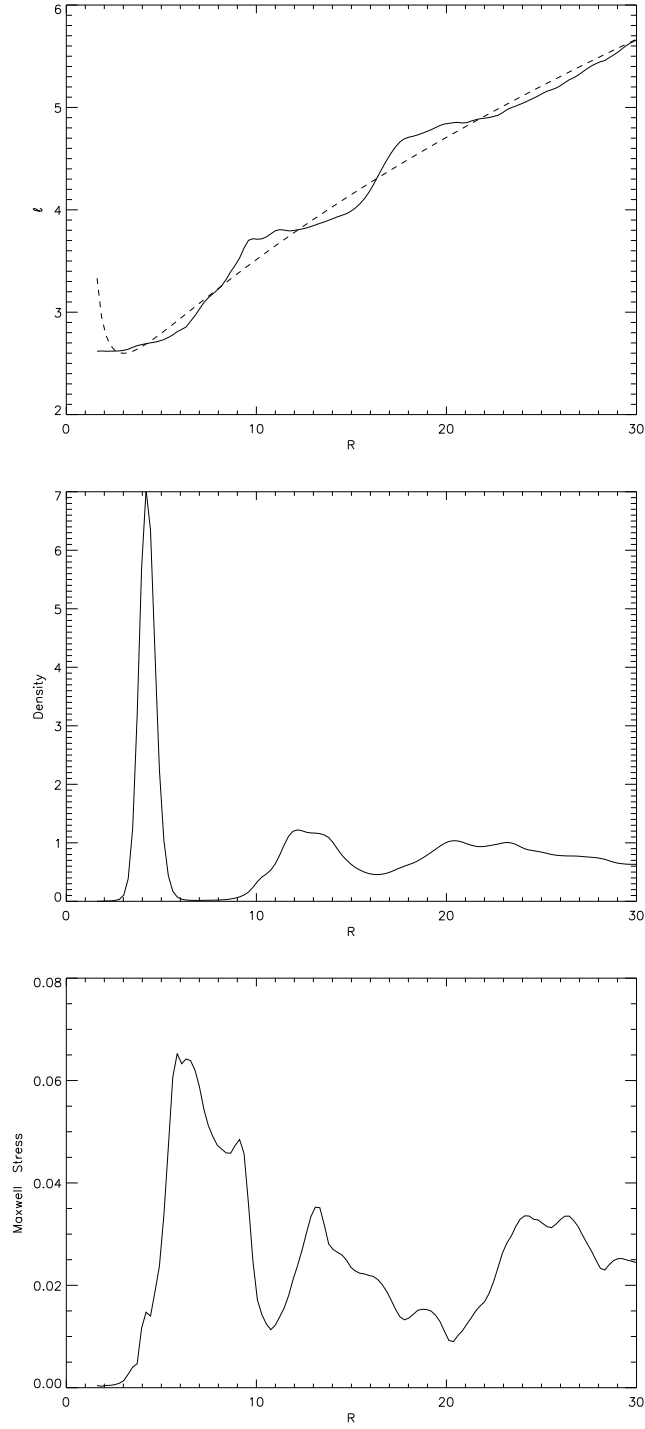


Fig. 4.— Vertically- and azimuthally-averaged values at $t = 4096$ in simulation CK6. (a) Specific angular momentum $\langle \ell \rangle$ overlaid on the Keplerian angular momentum (dashed line), (b) density $\langle \rho \rangle$, and (c) Maxwell stress normalized by the *initial* gas pressure, $M^{R\phi} / \rho c_s^2$.

As before, the large radial extent of this disk provides a reservoir of mass which will allow the inner region of the disk to evolve for many orbits without influence from the outer grid boundary.

For this simulation the initial state was relaxed to a true hydrodynamic equilibrium at the inner disk boundary. A constant density gas with $\rho = 1$ is first placed on the grid from $R = 4$ to the outer boundary. The initial sound speed is chosen to be $c_s = 0.086$ throughout the disk, corresponding to an isothermal scale height of 0.4 at $R = 4$ ($c_s^2/\Gamma = 0.01v_\phi^2$). This is hotter than the standard model of ARC ($c_s = 0.069$), but cooler than the thick disk model of HK. This initial condition is evolved in one dimension to an equilibrium solution. The resulting disk has $\rho = 1$ down to about $R = 7$, inside of which the density and pressure decline smoothly to zero at $R = 3$. Similarly, the angular momentum is Keplerian throughout most of the disk, but becomes slightly super-Keplerian as $R = 3$ is approached. The maximum increase over the Keplerian value is 3%.

A vertical magnetic field is placed onto this hydrodynamic equilibrium. As in run CK6 the field strength is set so that the Alfvén speed $v_A = \Omega/k_z$ for a wavenumber k_z corresponding to a wavelength of one quarter the vertical grid size. This is equal to $\beta = 276$ at $R = 4$ with β increasing to 10^6 by $R = 60$.

This disk is evolved for 270,000 timesteps out to a time $t = 2575$. This corresponds to 118 orbits at r_{ms} . Accretion through the inner boundary begins with a strong pulse at $t \sim 100$ as the magnetic instability in the inner part of the disk reaches nonlinear saturation. As the evolution proceeds, the location where magnetic instability is undergoing its initial linear growth moves out through the disk. The region that is in a quasi-steady state similarly moves out through the disk, albeit at a slower rate. The resulting disk can be described both in terms of instantaneous properties, which emphasize the turbulence and the fluctuations, or in terms of time- and space-averaged quantities which provide some measure of what the “steady state” properties of the disk are like.

Figure 5 shows the surface density distribution at the end time of the simulation. The most prominent features are the tightly wrapped trailing spiral waves. The spiral waves develop in the inner part of the disk along with the turbulence. A spacetime diagram shows that these waves propagate out through the disk at the sound speed. The waves are produced quasi-periodically throughout the evolution. A fourier transform of the accretion rate shows that the peak spectral energies correspond to the orbital period at $R = 6.7$ and 5.6 in the first half of the simulation, and larger radii at later times as the turbulence grows at those locations. The amplitude of the density fluctuations through these waves is measured by equation (8). Outside of $R = 20$ $\delta\rho/\rho \simeq 0.2$. Inside of this point, the fluctuation amplitude rises, reaching a value of 1.3 at r_{ms} . The accretion flow through r_{ms} tends to be highly nonaxisymmetric.

Of particular interest for this simulation is the magnitude of the stress at the marginally stable orbit, and its effect on the specific angular momentum ℓ . Throughout most of the disk the averaged ℓ tracks the circular orbit value, ℓ_{kep} , with a one to two percent excess over this value inside $R = 10$. Figure 6 shows the time evolution of both the Maxwell stress at r_{ms} in terms of the Shakura-Sunyaev α value defined with the local pressure, and the specific angular momentum

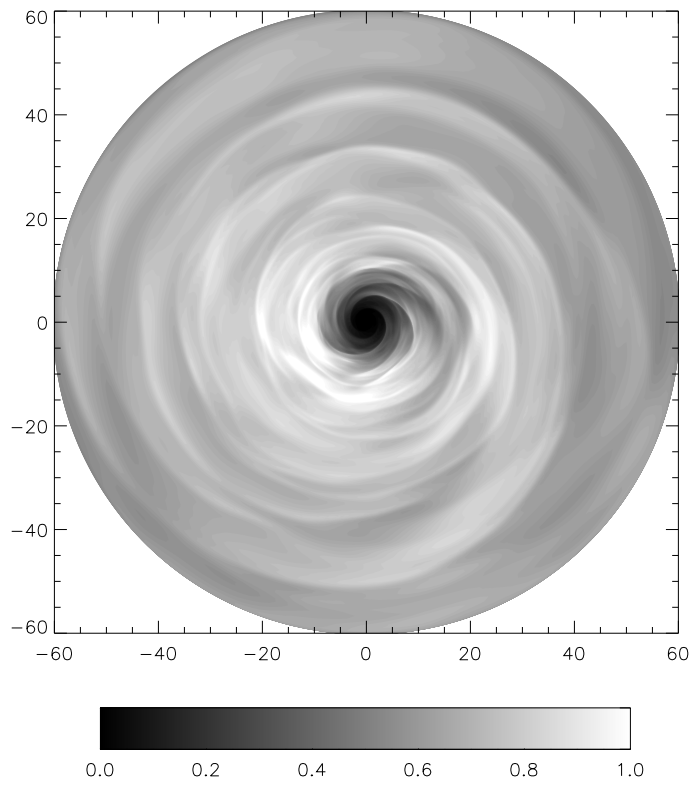


Fig. 5.— Vertically-averaged gas density in run CK7 at the end time $t = 2575$. The grey-scale is linear in density and runs from 0 to 1.

at r_{ms} and close to the inner boundary at $R = 1.66$. The first thing to notice is that the Maxwell stress at r_{ms} is nonzero and time-variable, as are the values of ℓ at r_{ms} and the inner boundary. There is, however, always a net change in ℓ between r_{ms} and the inner boundary. At r_{ms} , ℓ is always slightly greater than $\ell_{kep} \approx 2.6$; the time-average excess in the second half of the simulation is 1.8%. And although the slope $d\ell/dR$ decreases toward zero inside of r_{ms} , there is always an average decline in ℓ of 1.7% between r_{ms} and the inner radial boundary. This is smaller than the 5% drop reported by HK, but appears to be consistent with the results of ARC.

Figure 7 shows the ϕ - and z -averaged magnetic energies and the Maxwell stress as a function of radius averaged over the last 500 units of time. The values are scaled by the initial pressure. As always, the toroidal field energy is dominant, exceeding the radial field energy by a factor that declines with radius, from 20 at $R = 4$ to around 5 outside of $R = 15$. Inside $R = 3$, the radial field becomes more significant compared to the toroidal as the field is combed out by the nearly radial infall. The ratio of the toroidal to the vertical field energy is ~ 70 from $R = 10$ to 20, and rises rapidly both inside and outside this region. At r_{ms} $\beta = 8.5$; this increases with radius to $\beta \approx 100$ at $R = 20$. Note that the gas pressure is substantially reduced from its initial value inside of $R = 10$. The magnetic energy has grown by over 600 times from its initial value. Beyond $R = 20$ β rises more gradually to about 400 at the outer boundary.

The averaged mass accretion rate is relatively constant inside of $R = 15$ at late time. Beyond $t = 400$ the accretion rate into the central hole varies around a mean value of 0.072. The sense of accretion reverses at $R = 18$. The averaged radial drift velocity has the value $v_r/c_s \approx 0.008$ between $R = 10$ and 15, and rises rapidly to cross over $v_r/c_s = 1$ at $R = 2.6$; this is very similar to the velocity plot (Fig. 4) of ARC.

3.4. Influence of ϕ domain

One of the potentially most useful approximations for three-dimensional simulations is to reduce the azimuthal angular coverage to some integer fraction of 2π . The advantage of this is obvious: CK6 covered $\pi/2$ in 64 grid zones, whereas CK7 required 256 grid zones to span the full 2π with the same $\Delta\phi$. Model CK7a investigates the potential drawbacks of this reduction in computational domain size by providing a direct comparison between a simulation spanning $\pi/2$ and one spanning the full 2π (CK7). The grid size $\Delta\phi$ is the same in both simulations.

The two simulations are very similar in their qualitative appearance, although there are quantitative differences. CK7a has about 10% less magnetic energy and magnetic stress on average. On the other hand, CK7a exhibits larger fluctuations in those quantities. These differences carry over into the accretion rate into the black hole. In CK7 \dot{M} is 11% larger on average, but CK7a has larger impulsive spikes in accretion rate.

The larger fluctuation level seen in CK7a may be due, in part, to existence of the channel solution for vertical fields. Ideally the channels have a finite k_z and $k_R = m = 0$. However,

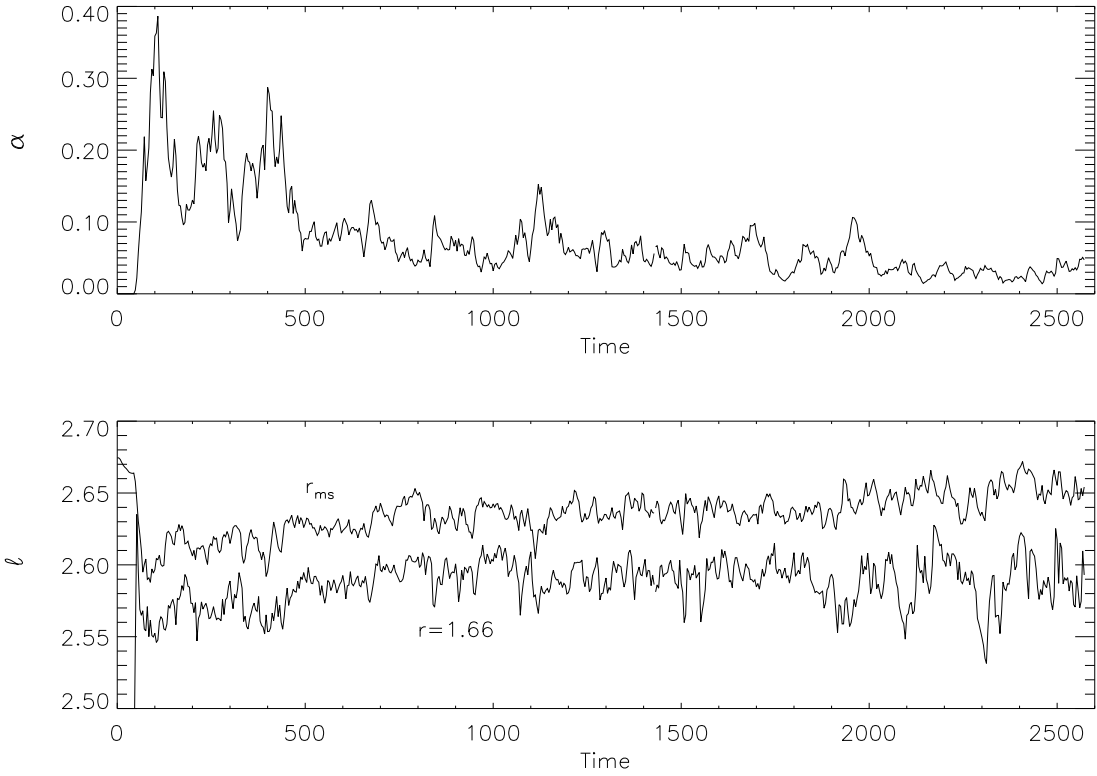


Fig. 6.— a) Maxwell stress $M^{R\phi}$ in CK7 at $R = r_{ms}$ as a function of time in terms of $\alpha = M^{R\phi}/P$, where P is the local gas pressure. (b) Time history of the specific angular momentum at $R = r_{ms}$ and $R = 1.66$. Although l varies considerably with time, there is always a small net change between r_{ms} and the inner radial boundary.

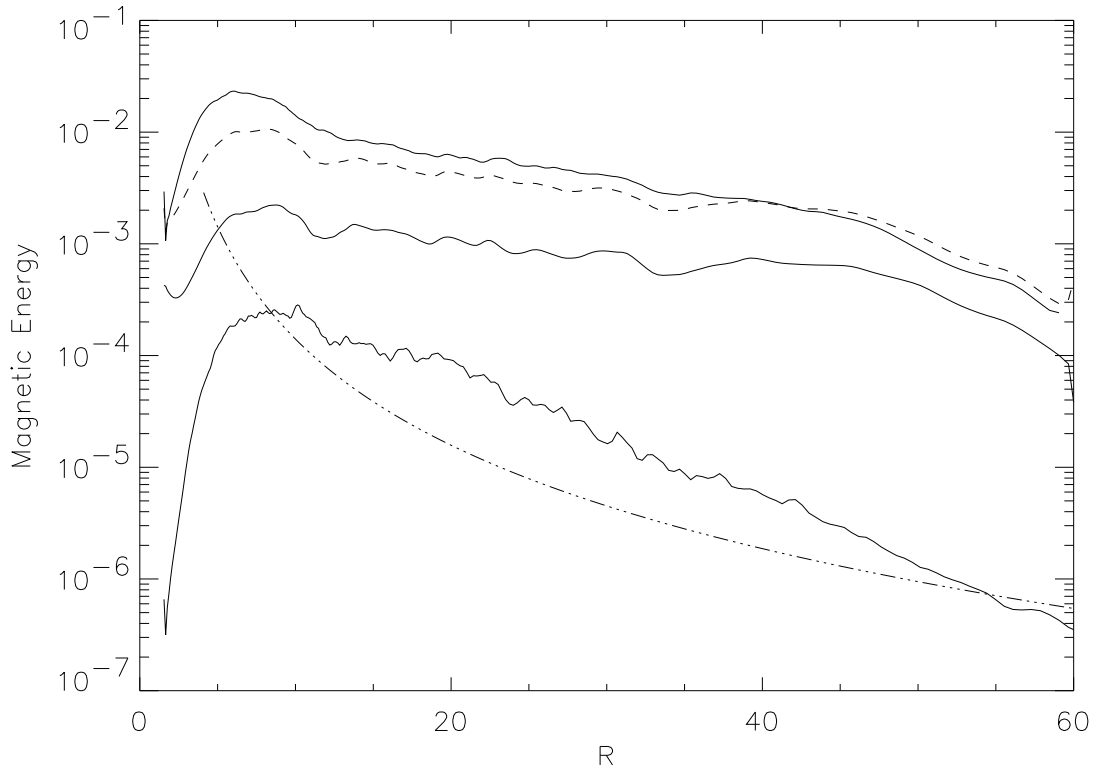


Fig. 7.— Magnetic energy averaged over ϕ , z , and the last 500 units of time in run CK7. The top solid curve is the toroidal field, the middle solid curve the radial field, the bottom solid curve the vertical field energy. The dashed line is the Maxwell stress, and the dot-dash line is the initial vertical field energy. All values are normalized with the initial gas pressure ($P = 0.0045$).

parasitic instabilities (Goodman & Xu 1994) with nonzero m and $k_R < k_z$ cause the breakup of the channel solution into smaller scale turbulence. Reducing the azimuthal extent of the computational domain apparently makes it easier for the channel solutions to maintain some spatial coherence for slightly longer time.

Does the reduced domain influence the amount of stress at the marginally stable orbit? The cylindrical disk simulations of ARC found a smaller decrease in specific angular momentum between r_{ms} and the inner boundary compared with the thick disk simulation of HK. Since ARC used an azimuthal domain of only $\pi/6$ in angle it is possible that some of the reduction in stress was due to the restricted angular domain. In CK7a the average α value at r_{ms} after $t = 1000$ is 0.053, although α does briefly go as high as 0.15 at several points in time. The mean value of ℓ at r_{ms} is 2.64 and the decrease between that point and the inner boundary is 0.032, or 1.2%. This is less than seen in CK7 (see Fig. 6), and is consistent with the general reduction in average stress levels in the reduced domain simulation. Thus, although the smaller domain size reduces the stress, this effect plays only a minor role in the quantitative differences in the simulations of HK and ARC.

As with CK7, the MHD turbulence produces propagating pressure waves. These are generated primarily in the inner portion of the disk at frequencies corresponding to the orbital frequency (rather than the periodicity frequency $\Omega/4$). These waves are tightly wrapped, low m trailing spirals. Figure 8a compares an angular power spectrum of density ρ for CK7 and CK7a at $t = 1500$. The spectrum is averaged over radius from $R = 5$ to 20. Both simulations show increasing power toward smaller azimuthal wavenumbers m . This is consistent with the visual appearance of the disk which in which low m spiral waves dominate. The steepness of the slope of the power spectrum increases with m , from ~ -2 at low m , up to ~ -7 for large m . The two simulations have very similar power spectra; CK7a is simply truncated by symmetry at $m = 4$.

The situation is somewhat different for the magnetic field. Figure 8b shows the azimuthal power spectra for the magnetic field components in runs CK7 and CK7a. What is most striking here is the break in the spectral slopes between $m = 10$ and 20. The same phenomenon was noted by Armitage (1998; see Fig. 3) in a full 2π simulation of a cylindrical disk with an initial vertical field. These plots suggest CK7 and CK7a are so similar because the primary input from the MRI is on scales $\sim H$, as would be expected for a vertical field, and $H \ll R$. The inverse cascade to smaller m numbers leaves CK7 with roughly 10% of the energy at the largest azimuthal scales, but this doesn't significantly alter the evolution of the MRI.

The azimuthal domain size might be more crucial in simulations of disks containing an initial toroidal magnetic field rather than a vertical field. With toroidal fields the instability depends directly upon the azimuthal wavenumber m . For example, the most unstable wavenumber has $m/Rv_A \approx \Omega$. For low m this corresponds to a field for which $v_A \sim v_\phi$, which would be an exceptionally strong field. Under such circumstances a full 2π global treatment would obviously be required. Even with weaker toroidal fields, when $v_A \ll v_\phi$, low m modes remain unstable, albeit with smaller growth rates. Further, in a shearing background, nonaxisymmetric waves have a time-

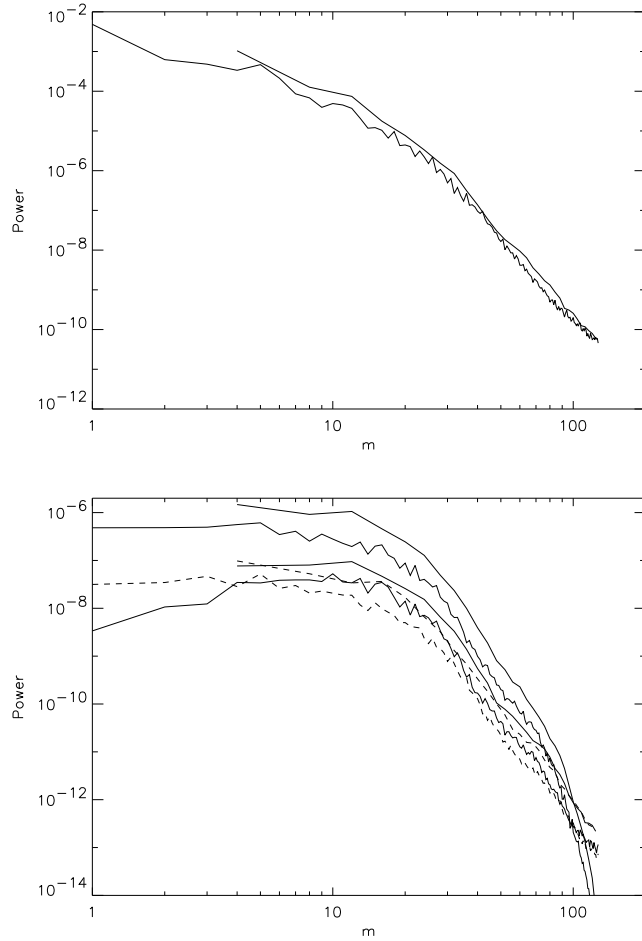


Fig. 8.— Azimuthal Fourier power spectra of (a) the vertically-averaged density, and (b) the magnetic field components B_R (lower solid curve), B_ϕ (top solid curve), and B_z (dashed curve). The data are taken from at the end time for CK7a (heavy curves) and the corresponding time in CK7, and averaged over space from $R = 5$ to 20. Density peaks at the smallest m wavenumbers, while the magnetic power spectra have a break in the slope between $m = 10$ and 20. In general, there is good qualitative agreement between the two simulations over their common angular domain.

dependent radial wavenumber. According to linear theory (Balbus & Hawley 1992; Terquem & Papaloizou 1996) for a given azimuthal mode m , maximum field amplification occurs when the the wavenumber quantity $(k/k_z)^2$ is small, hence field growth is maximized with low values k_R and/or high values of k_z . Since k_R evolves as $mtd\Omega/dR$ a reduction in total amplification can occur if low m modes are removed by a reduced angular domain size.

For a test comparison, we examine two cylindrical disk simulations that were computed for a separate project. These simulations are labeled NK1 and NK1a and are listed in Table 1. Each begins with identical initial conditions except that NK1a uses a $\pi/2$ angular domain and NK1 the full 2π . These simulations use a Newtonian gravitational potential with $GM = 1$ on a grid that runs from $R = 0.25$ to 3.75 , and 0 to 0.2 in z . Note that this make the time units different from the other runs; the orbital period at the center of the grid ($R = 2$) is 17.8 . The initial condition consists of an isothermal Keplerian disk. The temperature profile is fixed so that the Mach number $\mathcal{M} = c_s/v_\phi = 20$ is constant with radius. The pressure is also constant, and the density increases as R . The initial magnetic field is toroidal and of strength $\beta = 4$. The most unstable wavenumber is $m \cong v_\phi/v_A = \mathcal{M}\sqrt{2\beta} = 57$; this is well above the $m = 4$ limit of the $\pi/2$ grid.

Both simulations have a similar local growth rate for the perturbed magnetic field during the first few local orbital periods. Then the growth rate for NK1a drops off while NK1 continues unabated to saturation at a time of 10 local orbits. The field energy in NK1 is higher than in NK1a, but NK1a continues to grow with a slower rate, and manages to achieve about the same level as NK1 after 20 orbits. Beyond this point in time, the energies fluctuate around a mean, and the mean values differ by about 10%. Similarly, the mean magnetic stress in NK1a is 13% lower than in NK1.

An examination of the fourier power spectrum for the density and the magnetic field components in run NK1 shows that the power in the field components continues to rise until about $m = 4$. Beyond, to smaller m values, the power is flat (B_ϕ) or slightly decreasing (B_R). In contrast, the power in CK7 turns over at larger m values. The difference is that when the background field is toroidal there is power at $m = 0$. Further, the toroidal field is unstable for all nonzero m below the critical wavenumber $m = \sqrt{3}v_\phi/v_A$.

To conclude, although there are significant differences in the initial growth stage of the MRI, and there is power in the lowest m modes, by the end of the run the reduced domain size has the same effect on the toroidal field simulations as for those with vertical field: a 10% reduction in averaged field strengths. The reduction of the ϕ domain is a good approximation because the weak-field MRI is essentially a *local* instability. The MHD turbulence is driven locally, and the qualitative behavior of the disk is unchanged so long as the field remains weak, $\beta > 1$.

3.5. Equation of State

With the simple energy equation employed in these simulations there are two interesting limits: the adiabatic and the isothermal equations of state. Over the long term these two equations of state should lead to divergent evolutions as the adiabatic disk heats up. The present comparison has the modest goal of investigating whether the equation of state has an impact over a relatively brief period of initial evolution in the cylindrical disk.

Run CK7b is a repeat of CK7a using an isothermal equation of state. The initial linear growth phase in the two runs is essentially identical. Once turbulence sets in the runs vary in detail, but not in any systematic way. In particular there are no significant differences between the two runs in terms of stress at r_{ms} or the change in ℓ between r_{ms} and the inner boundary. Although the accretion rates in both runs differ from each other, they both also vary strongly in time, and the average difference between the two runs is less than the fluctuations level seen in either run alone.

The main differences observed in these two runs are consistent with what would be expected for these equations of state. In CK7a the temperature varies with radius, rising over the course of the simulation by as much as 30% inside of $R = 10$, while falling rapidly inside of r_{ms} . The temperature has also declined slightly outside of $R = 25$ due to expansion of the disk off the outer boundary. The density fluctuations (8) in the isothermal run CK7b are larger on average over the whole disk: the mean $\delta\rho/\rho$ is 0.73 versus 0.60 in CK7a.

4. A Hydrodynamic Disk

Cold disks such as protoplanetary disks may lack sufficient ionization to couple to the magnetic fields. What happens in a purely hydrodynamic disk? Since turbulence, angular momentum transport, and net accretion in disks result from the action of the MRI, evidence to date suggests that very little happens in such hydrodynamic disks. There is now a growing body of simulations (Stone & Balbus 1996; Balbus, Hawley & Stone 1996; Hawley, Balbus & Winters 1999; Godon & Livio 1999a) which are consistent with the conclusion that differentially rotating disks are hydrodynamically stable to both linear and finite-amplitude local perturbations. Although there is no particular reason to believe that *local* hydrodynamic stability properties would be altered in a fully global disk, the hydrodynamic disk nevertheless remains an important limiting test case to consider.

To follow the evolution of an initially turbulent disk in the *absence* of Lorentz forces, the output from CK5 at time $t = 3450$ is evolved forward in time (to $t = 4850$) purely hydrodynamically (run HK5). It is perhaps a bit self-inconsistent to ask how turbulence that is *generated* by magnetic fields subsequently evolves hydrodynamically. Of course when there is no self-consistent hydrodynamic turbulence, and one wishes to observe the hydrodynamic decay of turbulence, it is necessary to initialize the turbulence one way or another.

In any event, the results from HK5 are not surprising. After a brief period of readjustment to the loss of magnetic tension and pressure forces, the turbulent kinetic energies drop (Fig. 9). In particular, the vertical kinetic energy $1/2\rho v_z^2$ declines exponentially and the system became increasingly z -independent. This is consistent with the cylindrical limit and the Taylor-Proudman theorem which holds that in a steady, inviscid flow, slow motions in a rotating fluid should be two-dimensional. All accretion stops, and the inner edge of the disk readjusts slightly, moving outside of $R = 4$. Consistent with past local hydrodynamic simulations, there is no evidence for sustained turbulence or the development of any local hydrodynamic instability. Nor is there evidence for a strongly growing global mode.

Inward and outward propagating pressure waves are present throughout the simulation. These are in the form of tightly-wrapped trailing spiral waves, and they persist with constant or diminishing amplitude. A comparison of the azimuthal Fourier power spectrum for density from CK5 and HK5 finds that CK5 has more power for all wavenumbers m . The ratio of power in CK5 to HK5 rises from 2:1 at $m = 4$ (lowest wavenumber) up to 34:1 for $m = 44$. The high- m power in CK5 is driven by the MRI; its amplitude drops promptly with the elimination of the magnetic terms in HK5. The dominant $m = 4$ waves of HK5 appear to be driven mainly from the inner edge of the disk at frequencies close to the local orbital frequency there. The inner edge of the disk has a nonaxisymmetric structure that resembles a surface wave. This type of wave is seen to arise in Keplerian disks with a reflective inner boundary, and it is an example of a Papaloizou-Pringle instability (Godon & Livio 1999b). The pressure waves can, in principle, drive a small net inward drift within the disk. If one averages the accretion rate at each radius over the entire evolution there is a slight average inward accretion in the inner portion of the disk amounting to no more than $\dot{M} \sim 0.001$. A similarly averaged accretion rate in the magnetic disk is 0.075.

5. Discussion

5.1. Evolution of Keplerian disks: local versus global

The cylindrical disk is global in radius and azimuthal angle, but essentially local in z ; it represents the next step beyond local shearing box simulations. The first cylindrical disk was computed by Armitage (1998), and two cylindrical Keplerian disk models were computed in Hawley (2000), but the limited radial extent of the grid in these models restricted the amount of evolution possible before the outer boundary significantly affected the simulation. ARC computed three cylindrical disks with an initially gaussian density distribution, contained entirely upon the grid. They examine the inflow through the marginally stable orbit in a pseudo-Newtonian potential with an emphasis on the stress there. In this paper we consider the evolution of an MHD turbulent Keplerian cylindrical disks from simple initial conditions, but with a much larger radial extent.

First, how well do local shearing box simulations describe the state of the instability, turbulence, and transport due to the MRI when compared to global models? The answer seems to be

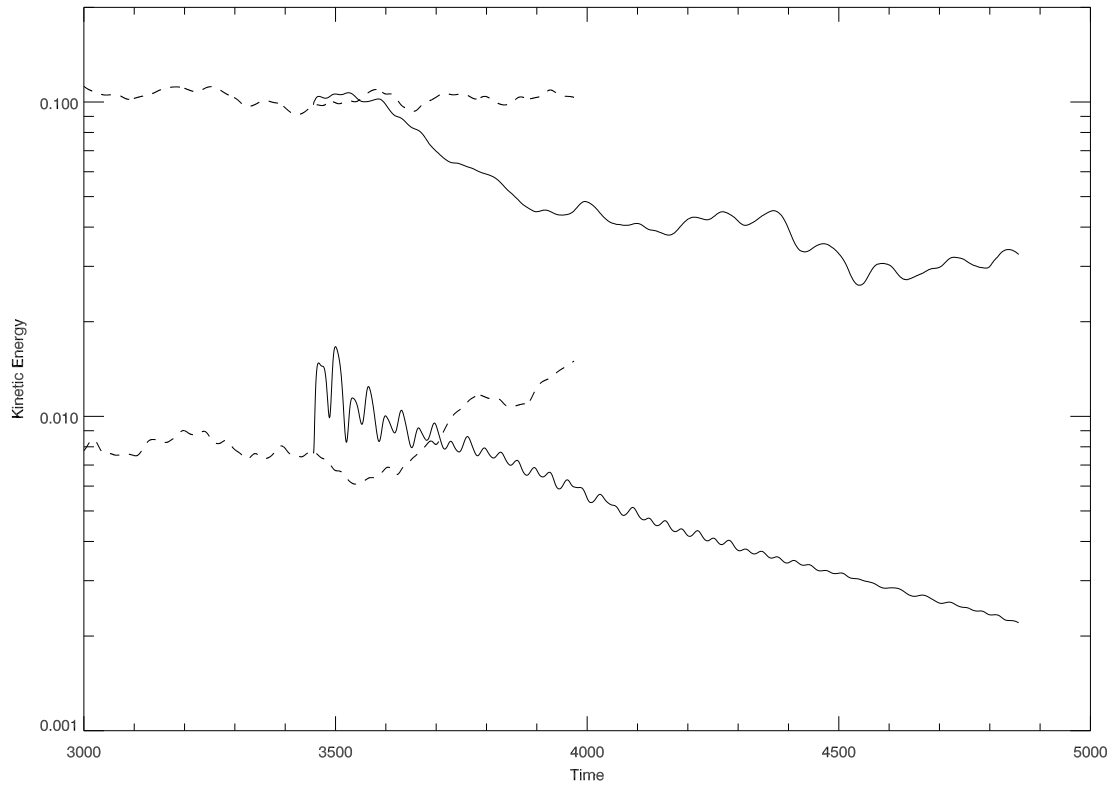


Fig. 9.— Time-history of the radial and vertical kinetic energy in MHD run CK5 (dashed line) and hydrodynamical run HK5 (solid line). HK5 begins from the data of CK5 at time $t = 3450$. After an initial readjustment to the loss of magnetic force, the kinetic energies in the hydrodynamic run decay away.

that local models do quite well, as long as the questions being asked of them are appropriate to the local approximation. Even in a global disk the MRI is a local instability; the wavelengths of the fastest growing modes are always less than H and R so long as the magnetic field is weak. The great similarity between the $\pi/2$ and 2π CK7 models illustrates this principle.

One of the major results from the local simulations is the importance of the background field topology. Local simulations (HGB95) find that a net vertical field leads to greater amplification of the initial field compared to a simulation beginning with a purely toroidal field. Stronger field amplification can lead to stronger turbulence and greater stresses. A comparison between models CK5 and CK6, and between as the vertical and toroidal simulations of ARC, support these conclusions in the global context as well. The “efficiency” of the Maxwell stress is measured by α_{mag} , the ratio of the Maxwell stress to the magnetic pressure. When the toroidal and radial field energies are comparable and the fields fully correlated to produce stress with the correct sign to transport angular momentum outward, $\alpha_{mag} \sim 1$. Simulations show that in both the global and local systems the turbulent state is dominated by toroidal field; this is particularly true when the initial background field is toroidal. With vertical initial fields the toroidal and radial fields are more comparable (although the toroidal field energy remains the largest). This is reflected in the values of α_{mag} : for vertical fields $\alpha_{mag} \approx 0.5$, while toroidal fields have a value closer to 0.3.

It should be mentioned that in the local simulations it is straightforward to measure the Reynolds stress, $\rho \delta v_r \delta v_\phi$; there is a well defined background shearing rate which allows an unambiguous definition of δv_ϕ as well as a limited volume over which to average. It is much more difficult to do this in the global simulations since at any given moment the background flow exhibits substantial deviations from, say, a Keplerian value. In local simulations, however, the Maxwell stress always dominates over the Reynolds stress by a factor of several. While measuring only the Maxwell stress for global simulations provides only a lower limit, $M^{R\phi}$ should nevertheless account for the majority of the stress.

Although the MRI is local and many properties of the resulting MHD turbulence are local as well, the stress is proportional to P_{mag} , the saturation amplitude of the field, and this might well be determined by global properties such as the scale height H or the ratio H/R . So far this has been difficult to assess. The traditional Shakura-Sunyaev α parameter is set by the relation $\alpha = \alpha_{mag}/\beta$. Thus $\alpha = 0.1$ – 0.01 requires $\beta \sim 3$ – 50 . In local simulations vertical fields tend to saturate near the lower end of this β range, and toroidal fields at the upper end, unless the toroidal field *began* with $\beta \sim 1$ – 10 . If one considers the current global simulation results, both from this paper and from previous cited works, the impression is that global simulations produce lower β at saturation and larger α values than the local models. However, one should be cautious drawing a general conclusion at this stage. The global simulations have initial vertical fields (or poloidal field loops), or initially strong toroidal fields. For such fields the resulting saturation levels near $\alpha \sim 0.1$ are fully consistent with the local simulations. Local simulations saturate at higher β values when the initial field consists of weak random field, or weak toroidal field, and these cases have not yet been investigated globally, in part due to the higher resolution required.

One aspect that emerges from these and other global simulations is the difficulty of characterizing a “steady state” disk. In the global simulations all quantities vary strongly both in time and in space. Although one can average over space and over many orbits and obtain relatively smooth spatial distributions, significant fluctuations are always present.

Absent from the local models, but present in global disks are effects such as a net accretion and spiral wave propagation. The MRI is inherently time unsteady and produces fluctuations in the disk at frequencies close to the local orbital frequency, generating magnetoacoustic waves. It not surprising that strong MHD turbulence should generate such magnetoacoustic waves. Blaes and Balbus (1994) show that the presence of toroidal fields couples the compressible and incompressible modes of the MRI, and when β approaches order unity, significant acoustic modes are expected. In These spiral waves are generated at small radii and propagate out through the full radial extent of the disk. This is one way that the turbulence at the inner part of the disk exerts a global effect on the disk.

5.2. Viscous Instability

A prominent feature of model CK6 at late time is the presence of a dense ring in the inner region and low density gaps that have formed within the disk. These gaps arise due to a type of “viscous” instability, specifically an inverse relationship between the Maxwell stress and the density. Although these rings and gaps are most prominent in CK6, there is evidence for a similar tendency in CK5, the toroidal field simulation.

The dense rings that form in CK6 are likely to be enhanced by the cylindrical approximation. The rings *per se* might not form in simulations with vertical stratification since the strong magnetic field located between the dense rings would be buoyant. Cylindrical symmetry eliminates the possibility of buoyancy as well as any development of magnetized outflows. The tendency for greater stress in regions of lower density is not due to the cylindrical limit, however, but due to the increased Alfvén speeds in such regions. The probable outcome of this tendency in stratified disks will be larger stresses in the lower density region above the equatorial plane (see, for example, in the simulations of Miller & Stone 2000), and the creation of local regions of strong toroidal field that will be ejected into a corona. In fact, strong toroidal fields rising out of the disk are a common feature of the global thick torus simulations of Hawley (2000), HK, and Machida et al. (2000). Another consequence is that the accretion rate through the disk will be inherently unsteady, and spatially inhomogeneous. The two-dimensional axisymmetric global MHD simulations of Stone & Pringle (2000), for example, provide evidence of just such strong radial inhomogeneities in accretion rate and density.

How generic is this tendency to develop a viscous instability? Interestingly there is no evidence for the formation of dense rings in CK7, in contrast to CK6. The most obvious systematic differences between CK6 and CK7 are the domain size ($\pi/2$ versus 2π), the equation of state (isothermal

versus adiabatic), the absence or presence of net accretion into the central hole, and total evolution time. The influence of the ϕ domain seems too small to account for the difference. Although an isothermal equation of state can create greater density fluctuations, a direct comparison between adiabatic and isothermal models CK7a and CK7b does not find any systematic effect due to the choice of equation of state. Further, ARC used an isothermal equation of state and did not observe any tendency toward the formation of dense rings.

This leaves the influence of the inflow through the marginally stable orbit and the duration of the simulation. In models that do not accrete through the marginally stable orbit, mass tends to pile up at the inner edge of the disk. The accretion through r_{ms} prevents this, and creates an inward pointing pressure gradient out through the disk to radii that are several times r_{ms} . This appears to inhibit the development of the viscous instability, at least in the inner disk over the time scales simulated. The viscous instability might yet manifest itself in the disk at larger radii, but CK7 was not run far enough in time for this to occur. Further simulations and analysis would be required to test this conjecture further.

5.3. Stress at the Marginally Stable Orbit

Since the pseudo-Newtonian potential is used for these simulations, we can examine the evolution of the stress and specific angular momentum in the region of the marginally stable orbit. The cylindrical simulations demonstrate that the stress is continuous at r_{ms} ; indeed, there is nothing special at the precise location of r_{ms} in any disk quantity. In the present simulations the slope of the specific angular momentum $d\ell/dR$ inside the marginally stable orbit is smaller than seen in the fully global thick disk simulations of Hawley (2000) or HK. The slope is close to that reported by ARC from their simulations of cylindrical Keplerian disks. What then determines the degree to which ℓ is reduced inside of r_{ms} ? In each case there is some nonzero stress inside of r_{ms} . Naturally, larger stresses have a larger effect. The question becomes what circumstances produce those larger stresses?

A reduced angular computational domain lowers the observed stress levels, but only by about 10%. The use of an isothermal versus adiabatic equation of state apparently has even less influence, at least when the temperatures at r_{ms} are comparable. The internal pressure may have a greater influence, by increasing the radial distance inside of r_{ms} where the flow remains subsonic, however there is only circumstantial evidence for this in the results to date. The simulations run here were about half as hot as those of HK, and comparable to the fiducial runs of ARC. ARC also ran a simulation with the sound speed cut in half but did not report any significant differences in the results.

Possibly the most important approximation is the use of cylindrical geometry in lieu of full stratification. Stratified simulations find that the largest magnetic field strengths and Alfvén speeds occur in the lower density regions surrounding the equator (Miller & Stone 2000). In the thick disk

simulation of HK the specific angular momentum was nearly constant inside of r_{ms} along the equator. The strongest fields and stresses were located above and below the equator, and this is where the greatest reduction in ℓ occurred. To investigate this further there appears to be no substitute for stratified global simulations.

5.4. Hydrodynamic Stability

Repeated local simulations have failed to find any evidence for a purely hydrodynamic local nonlinear instability. The absence of magnetic fields has always resulted in the decay of any imposed turbulence, leading to the conclusion that there is no turbulent α in unmagnetized disks. While there are known global instabilities in hydrodynamic disks such as the Papaloizou-Pringle instability, or local violations of the Høiland criteria, the circumstances under which these manifest themselves are known, and these instabilities are unlikely to be generally significant.

As a control a hydrodynamic cylindrical disk is computed. This disk begins with a Keplerian disk that is MHD turbulent. The simulation consists of turning off the magnetic forces and following the subsequent hydrodynamic evolution. The outcome is straightforward: the disk turbulence dies out promptly. All vertical structure decays away and the disk becomes two dimensional. Global spiral waves continue to propagate, but their amplitudes are reduced from those seen with active MHD, particularly for larger azimuthal wavenumbers.

5.5. Coherent structures

Another issue of interest in disks, hydrodynamic or magnetohydrodynamic, is the possible formation of coherent structures. For example, Abramowicz et al. (1992) suggested that coherent vortices might produce observable modulations in the luminosity of disks in active galaxies. More recently, vortices have been proposed as sites for planetesimal formation in protoplanetary disks.

Two-dimensional (R, ϕ) hydrodynamic simulations of Keplerian disks have been carried out by Nauta & Tóth (1998), Nauta (1999), and Godon & Livio (1999b; 2000). The results to date can be summarized thusly: (1) vortices placed in hydrodynamic Keplerian disks can survive for many orbits, and (2) vortices have not been observed to arise spontaneously in initially Keplerian disks. Point (1) is quite understandable since the counter-rotating epicyclic flow is an equilibrium solution. Point (2) follows from the stability of a hydrodynamic Keplerian flow; there is nothing to drive the transition.

These points are illustrated by an example where coherent hydrodynamic structures *were* observed to arise in simulations of globally unstable disks. This is the counter-rotating coherent “planet” discovered by Hawley (1987) in simulations of the nonlinear saturation of the Papaloizou & Pringle (1984) instability in slender tori. Planets form in thick accretion tori as well (Hawley

1991), although in a less dramatic fashion than in the slender torus limit. These structures were described analytically by Goodman, Narayan, & Goldreich (1987) as fluid undergoing elliptical counter-rotating epicyclic motion. In these planets the Coriolis force is in balance with the fluid pressure, creating an equilibrium structure. These structures can be described as vortices, but the essence of their nature is epicyclic motion. While they are a local equilibrium solution for a differentially rotating fluid, it is unclear when such solutions can arise from an initially axisymmetric disk flow. In the slender torus, the epicyclic planets develop through the action of the Papaloizou-Pringle instability. The instability triggers the transition from one equilibrium to the other. The prospects for such a transition in a stable Keplerian disk seem less promising.

In run HK5 there is no sign of emerging or sustained coherent structures such as counter-rotating epicyclic flows. When looking for coherent structures, however, it is hardly necessary to confine one’s attention to hydrodynamic disks. We can also ask whether self-sustained MHD turbulence generates coherent structures. No such structures have been observed in local simulations (e.g., Brandenburg et al. 1995). Similarly, in global MHD simulations, cylindrical or otherwise, there has been no evidence for the formation of coherent structures.

It is worth reiterating that the coherent vortices, i.e., the hydrodynamic planet structures, owe their existence to the presence of stable epicycles, but it is precisely those epicycles that are disrupted by the action of the MRI. Still, analytic MHD equilibrium coherent structures have been found by Balbus & Ricotti (1999) in the local limit which are magnetic analogues to the hydrodynamic planet solution. It has yet to be demonstrated that these solutions are stable, or that they can develop in an MHD disk.

5.6. Impact of numerical model assumptions

Given the demands of three dimensional simulations, it is useful to explore ways in which the global problem can be restricted without too much loss of significance. One such simplification is the cylindrical disk limit, and another is the restriction to a smaller domain in ϕ . This paper has examined the influence of the later approximation for a model with an initial vertical field, and one with an initial toroidal field.

The explicit comparison between simulations using the full 2π and ones that span only $\pi/2$ in angle suggests that the restricted azimuthal domain is indeed a useful approximation. The vertical field simulations are qualitatively very similar throughout. Although the initial growth stage in the toroidal field cases are noticeably different in the two different computational domains, the final turbulent states are again very similar. With vertical fields the magnetic azimuthal power spectrum has a significant break at relatively high m wavenumbers, consistent with the fastest growing modes of the vertical MRI. With toroidal fields the power spectra level out toward low m and do not show the same break. Again, this is consistent with the MRI: weak toroidal fields are unstable for all m less than $\approx v_\phi/v_A$. In either case, however, the power spectra of the 2π

and $\pi/2$ simulations are very similar where their wavenumbers overlap. Total stress and accretion rate values are reduced by about 10% in the restricted domains, indicating that 10% of the energy is to be found on the largest azimuthal scales. This is not entirely negligible, but the qualitative difference does not appear to be profound.

A significant factor in global simulations remains the grid resolution which will always fall short of what one can achieve with a local simulation. Here the average radial grid zone size is $\Delta R = 0.23$. The standard radial resolution in the local simulations of HGB95 was almost a factor of 10 better. Because of the lack of stratification, the vertical resolution in the cylindrical simulations is comparable to the local model. A resolution comparison done by HK found larger magnetic energies with better resolution, a result consistent with more detailed resolution studies in the local shearing box. Even with the grid resolution that is presently possible, however, global simulations generate and maintain MHD turbulence with physically significant stress levels.

6. Conclusion

Cylindrical disk simulations are a useful tool for investigating global evolution of disks evolving due to magnetically driven turbulence. Such simulations demonstrate that the conclusions developed in the local shearing box model hold in the global context as well. As in the local model the MRI grows rapidly and produces MHD turbulence with a significant Maxwell stress. The turbulence is more vigorous and more efficient in producing stress for a given total magnetic pressure when driven by an initial field that is vertical rather than toroidal. Hydrodynamics alone seems no more effective at creating or sustaining turbulence in a global model than it is in a local one.

In addition to reaffirming local properties of the MRI, cylindrical disk simulations illuminate disk characteristics that are truly global. A net accretion rate is one such property, but there are also important nonlocal structural features. Tightly-wrapped low- m spiral waves are prominent. The final accretion through the marginally stable orbit provides an example of a highly nonaxisymmetric spiral flow. Particularly interesting in the present simulations is the tendency for radial variations in Maxwell stress to concentrate gas into rings, creating substantial spatial inhomogeneities.

A perennial question is the degree to which these simulations resemble traditional steady state α -disk models. They do in so far as they accrete in direct response to internal stress, specifically due to MHD turbulence. Beyond that, however, there are significant differences. The simulations are characterized by large scale variability in space and time in all variables. The stress is proportional to the magnetic pressure which is itself only indirectly related to other disk parameters. In the simulations it is possible to approximate a quasi-steady state only with broad-stroke averages. In part this is due to the initial conditions (e.g., isolated tori or constant density slabs) which are far from a possible accreting steady state solution. To address this issue it will be useful to attempt simulations that begin with more realistic initial states. Results to date indicate, however, that analytic disk models are likely to prove woefully inadequate in describing detailed spatial and

temporal disk properties so long as they are based upon a strict α formulation with α a constant in space and/or in time.

Although cylindrical disk simulations provide a valuable point of reference for future work, the lack of vertical stratification is clearly a major limitation for investigating many important physical processes. This is obviously true for the development of a magnetized corona, or the launching of winds or jets. It appears also to be an important factor in measuring the stress in the disk at the marginally stable orbit. Stratified global thin disk simulations are the next logical step to contrast with existing global thick disk models. Stratified thin simulations will require far more vertical grid zones centered around the equator than are used in cylindrical disks. However, the tests presented here suggest that a reduction in the ϕ domain is an acceptable problem simplification, as long as the potential for some small quantitative reduction in energy levels is kept in mind.

I thank Steve Balbus, Julian Krolik, Jim Stone, and Wayne Winters for useful discussions related to this work. Wayne Winters supplied data from his unpublished simulations NK1 and NK1a for the analysis in §3.4. This work was supported by NSF grant AST-0070979, and NASA grants NAG5-9266 and NAG5-7500. Simulations were carried out on the Cray T3E and T90 systems of the San Diego Supercomputer Center of the National Partnership for Advanced Computational Infrastructure, funded by the NSF.

REFERENCES

- Abramowicz, M. A., Lanza, A., Spiegel, E. A., & Szuszkiewicz, E. 1992, *Nature*, 351, 41
- Armitage, P. J. 1998, *ApJ*, 501, L189
- Armitage, P. J., Reynolds, C. S., & Chiang, J. 2001, *ApJ*, in press (ARC)
- Balbus, S. A., & Hawley, J. F. 1991, *ApJ*, 376, 214
- Balbus, S. A., & Hawley, J. F. 1992, *ApJ*, 400, 610
- Balbus, S. A., J. F. Hawley, & J. M. Stone 1996, *ApJ*, 467, 76
- Balbus, S. A., & Ricotti, M. 1999, *ApJ*, 518, 784
- Blaes, O. M., & Balbus, S. A. 1994, *ApJ*, 421, 163
- Brandenburg, A., Nordland, Å., Stein, R. F., & Torkelsson, U. 1995, *ApJ*, 446, 741
- Godon, P., & Livio, M. 1999a, *ApJ*, 521, 319
- Godon, P., & Livio, M. 1999b, *ApJ*, 523, 350
- Godon, P., & Livio, M. 2000, *ApJ*, 537, 396

- Goodman, J., Narayan, R., & Goldreich, P. 1987, MNRAS, 225, 695
- Goodman J., & Xu, G. 1994, ApJ, 432, 213
- Hawley, J. F. 1987, MNRAS, 225, 677
- Hawley, J. F. 1991, ApJ, 356, 580
- Hawley, J. F. 2000, ApJ, 528, 462
- Hawley, J. F., & Balbus, S. A. 1992, ApJ, 400, 595
- Hawley, J. F., Balbus, S. A., & Winters, W. F. 1999, ApJ, 518, 394
- Hawley, J. F., Gammie, C. F., & Balbus, S. A. 1995, ApJ, 440, 742 (HGB95)
- Hawley, J. F., Gammie, C. F., & Balbus, S. A. 1996, ApJ, 463, 656
- Hawley, J. F., & Krolik, J. H. 2001, ApJ, 548, in press (HK)
- Hawley, J. F., & Stone, J. M. 1995, Comp Phys Comm, 89, 127
- Lightman, A. P., & Eardley, D. M. 1974, ApJ, 187, L1
- Machida, M., Hayashi, M. R., & Matsumoto, R. 2000, ApJ, 532, L67
- Matsumoto, R. 1999, in Numerical Astrophysics, eds. Miyama, S., Tomisaka, K. & Hanawa, T (Kluwer: Dordrecht), 195
- Matsumoto, R., & Tajima, T. 1995, ApJ, 445, 767
- Miller, K., & Stone, J. M. 2000, ApJ, 534, 398
- Nauta, M. D. 1999, PhD thesis
- Nauta, M. D., & Tóth, G. 1998, A&A, 336, 791
- Paczynski, B., & Wiita, P. J. 1980, A&A, 88, 23
- Papaloizou, J. C. B., & Pringle, J. 1987, MNRAS, 208, 721
- Shakura, N. I., & Sunyaev, R. A. 1973, A&A, 24, 337
- Stone, J. M., & Balbus, S. A. 1996, ApJ, 464, 364
- Stone, J. M., & Norman, M. L. 1992a, ApJS, 80, 753
- Stone, J. M., & Norman, M. L. 1992b, ApJS, 80, 791
- Stone, J. M., & Pringle, J. 2000, MNRAS, in press

Terquem, C., & Papaloizou, J. C. B. 1996, MNRAS, 279, 767

TABLE
CYLINDRICAL KEPLERIAN DISK SIMULATIONS

Model	(R, ϕ, z) Domain	Grid	Equation of State	Initial Field	End time
CK5	1.5-61.5, $\pi/2$, 2.0	$256 \times 58 \times 24$	isothermal	toroidal	3972
HK5	1.5-61.5, $\pi/2$, 2.0	$256 \times 58 \times 24$	isothermal	hydro	1400
CK6	1.5-61.5, $\pi/2$, 2.0	$256 \times 64 \times 32$	isothermal	vertical	4097
CK7	1.5-61.5, 2π , 0.8	$256 \times 256 \times 32$	adiabatic	vertical	2575
CK7a	1.5-61.5, $\pi/2$, 0.8	$256 \times 64 \times 32$	adiabatic	vertical	1500
CK7b	1.5-61.5, $\pi/2$, 0.8	$256 \times 64 \times 32$	isothermal	vertical	1500
NK1	0.25-3.75, 2π , 0.2	$128 \times 128 \times 32$	isothermal	toroidal	71.1
NK1a	0.25-3.75, $\pi/2$, 0.2	$128 \times 32 \times 32$	isothermal	toroidal	66.6